Title
Atomic and nano-scale characterization of a 50-year-old hydrated C3S paste

Authors
Geng, G
Taylor, R
Bae, S
et al.

Publication Date
2015-07-17

DOI
10.1016/j.cemconres.2015.06.010

Peer reviewed

Cement and Concrete Research 77 (2015) 36–46

Contents lists available at ScienceDirect

Cement and Concrete Research

journal homepage: http://ees.elsevier.com/CEMCON/default.asp

Atomic and nano-scale characterization of a 50-year-old hydrated C_3S paste

Guoqing Geng [a], Rae Taylor [a], Sungchul Bae [a], Daniel Hernández-Cruz [c], David A. Kilcoyne [b], Abdul-Hamid Emwas [d], Paulo J.M. Monteiro [a,*]

[a] Department of Civil and Environmental Engineering, University of California at Berkeley, United States
[b] Advanced Light Source-Lawrence Berkeley National Laboratory, Berkeley, CA, United States
[c] Facultad de Ingeniería, Universidad Autónoma de Chiapas, Tuxtla Gutiérrez, Chiapas 29050, Mexico
[d] NMR Core lab, King Abdullah University of Science and Technology, 23955 Thuwal, Saudi Arabia

ARTICLE INFO

Article history:
Received 21 October 2014
Accepted 22 June 2015
Available online xxxx

Keywords:
TEM (B)
NMR
Microstructure
Ca_3SiO_5 (D)
STXM

ABSTRACT

This paper investigates the atomic and nano-scale structures of a 50-year-old hydrated alite paste. Imaged by TEM, the outer product C–S–H fibers are composed of particles that are 1.5–2 nm thick and several tens of nanometers long. ^{29}Si NMR shows 47.9% Q_1 and 52.1% Q_2, with a mean SiO_4 tetrahedron chain length (MCL) of 4.18, indicating a limited degree of polymerization after 50 years' hydration. A Scanning Transmission X-ray Microscopy (STXM) study was conducted on this late-age paste and a 1.5 year old hydrated C_3S solution. Near Edge X-ray Absorption Fine Structure (NEXAFS) at Ca $L_{3,2}$-edge indicates that Ca^{2+} in C–S–H is in an irregular symmetric coordination, which agrees more with the atomic structure of tobermorite than that of jennite. At Si K-edge, multi-scattering phenomenon is sensitive to the degree of polymerization, which has the potential to unveil the structure of the SiO_4^{4-} tetrahedron chain.

1. Introduction

Portland cement is the primary component of modern concrete, and its use in construction continues to increase [1]. Despite decades of research, many questions regarding the hydration and long-term performance of cement-based materials remain unclear. One of the key issues that remain to be resolved is the atomic, nano- and micro-scale structures of hydration products, particularly calcium silicate hydrates (C–S–H). Answers to these questions are critical to improving modern concrete science and technology.

Relevant research is hamstrung by the complexity of the cement-based material, which comes from the heterogeneous nature of the hydration products of ordinary Portland cement (OPC). Alite, or its pure chemical phase tricalcium silicate ($3CaO \cdot SiO_2$, or, in cement chemistry notation, C_3S), is a major component of OPC and is frequently used to model the hydration system of OPC [2,3]. However, even when modeling a simple system such as pure C_3S, the dissolution, diffusion and precipitation processes involved in the hydration process still remain unclear.

For example, the heat evolution of C_3S hydration shows an induction behavior between the initial heat release (shortly after mixing with water) [4,5] and accelerated reaction period, which cannot be thoroughly explained by any single hypothesis. Stein [6] was the first researcher to attribute this induction behavior to the rapid formation of a meta-stable calcium silicate hydrate layer, which is thin but able to prohibit the dissolving of unreacted C_3S. Thomas [2] has suggested that the slow rate of nucleation on C_3S surface could solely account for the phenomena. This hypothesis gives a more robust interpretation of the heat evolution compared to the Avrami model, which is based on random nucleation [7].

If debates in the mechanism of hydration behavior remain unresolved, they pale in comparison to the contentious discussions surrounding the nature of the primary hydration products, calcium silicate hydrates (C–S–H). At the atomic scale, Taylor [8] suggested a dreierketten structure based on the natural mineral tobermorite ($Ca_5Si_6O_{16}(OH)_2 \cdot 4H_2O$). Any observed high Ca/Si atomic ratio in C–S–H could be explained by either a shortening of chain length or the incorporation of calcium hydroxide and a natural calcium silicate hydrate mineral, jennite ($Ca_9Si_6O_{18}(OH)_6 \cdot 8H_2O$). The NMR [9] study of neat C_3S hydration indicates that the mean chain length (MCL) of the SiO_4^- tetrahedron chain is about 2 at early age and 4.76 after 26 years of hydration. Based on Taylor's model, Richardson [10] developed a more explicit model that attempts to explain several experimental observations, such as the alternation of Ca/Si ratio and the evolution of MCL during hydration. At the nano-scale, Jennings [11] suggested that the basic construction unit of C–S–H is a non-spherical globule whose dimension is around 5 nm. Constantinides and Ulm [12] applied this model successfully to

* Corresponding author. Tel.: +1 510 643 8251; fax: +1 510 643 5264.
E-mail address: monteiro@berkeley.edu (P.J.M. Monteiro).

http://dx.doi.org/10.1016/j.cemconres.2015.06.010
0008-8846/

their nano-indentation experiments. The TEM studies of hydrated C_3S and pozzolanic material by Richardson [10] and Taylor [13] demonstrated that the outer product of hydrated C_3S grain, at high Ca/Si ratio, is composed of long-thin particles but two-demensional foils in case of low Ca/Si ratio; the inner product is rather featureless.

In this paper, we denote "outer product" as the hydrates that form in the space that was originally occupied by water, and "inner product" as the hydrates that form within the original boundary of C_3S and water. As described by Richardson [10], in an 8-year-old C_3S paste with water/cement ratio (w/c) = 0.4 hydrated at 20 °C, large fibrillar outer products C–S–H (Op C–S–H) form in a radial fashion, rooting on the boundary between Op and Ip C–S–H. Each fibril (100–150 nm wide) is composed of a finer substructure also in a fibrillar shape. This substructure is about 3 nm in its smallest dimension, with the length varying from a few nanometers to many tens of nanometers.

The sample being investigated here is a 50-year-old alite (96% C_3S) hydration system with w/c = 0.5. Most research in cement hydration is limited to a three-year window of time [14]. Analyses of hydration periods greater than this are rarely reported or conducted, even though the typical design service life cycle of cementitious material is, on average, 50 years and sometimes as long as 100 years. Therefore, analysis of the evolution of cementitious material at very late age is critical to determine its chemical composition, microstructure and macro-performance.

Previous reports of NMR results on late age samples [10,9,14] indicate elongation in MCL. To advance the limited knowledge of the mechanisms governing late-age hydration, the research reported herein analyzed a 50-year-old paste using the unique characterizing technique, Scanning Transmission X-ray Microscopy (STXM), combined with similar techniques to those described in literature. The STXM combines X-ray microscopic capabilities with Near Edge X-ray Absorption Fine Structure (NEXAFS) spectroscopy, enabling the in-situ investigation of Si and Ca coordination environments within the cementitious material. STXM has been proven useful for examining cement hydration [15,16], but this is the first study to utilize sample at late age hydration.

2. Experimental methods

2.1. Sample preparation

Synthesized alite (96% C_3S [17]) and distilled water were mixed at w/c = 0.5, and cast into a 2-inch-long, 0.5-inch-diameter cylindrical mold. For the first three years the sample was stored in saturated $Ca(OH)_2$ water solution at room temperature. After that the sample was kept in a sealed plastic container, cured at room temperature for 47 years. To investigate the evolution of C–S–H, a 1.5-year-old sample was also prepared by mixing pure C_3S with distilled water at w/c = 5.0. Such a high water to cement ratio was used, so that the suspension could be studied by STXM in an in-situ way. Hydrated C_3S particles were kept in their original morphology.

2.2. X-ray diffraction (XRD)

X-ray diffraction was performed with PANalytical X'Pert Pro diffractometer, operating at 40 keV and 40 mA with a Cobalt anode. The 2-theta scanning range was between 5° and 100°, with a step width of 0.0167° and collection time of 0.475 seconds per step. Software *HighScore (Plus)* was used to identify the peak positions. There is an increased possibility of carbonation since the sample was stored for 50 years. To identify the carbonation status, two powder samples were prepared for the XRD test, one from the surface of the cylinder and the other from the core, denoted respectively as SP (surface part) and CP (core part).

2.3. Scanning Electron Microscope (SEM)

This study used a ZEISS EVO® MA10 SEM, with an Energy Dispersive X-ray Spectrometer (EDX), operated in the Secondary Electron (SE) detection mode with high vacuum and an accelerating voltage of 20 kV. Probe currency was modified to obtain the best image quality. In order to avoid carbonation, only sections of the sample taken from the core were viewed under the SEM. The natural fracture surface of the sample was carbon-coated to prevent sample charging, while various locations were observed to yield a statistically representative result.

2.4. ^{29}Si Magic Angle Spinning Nuclear Magnetic Resonance (MAS-NMR)

A section of the sample taken from the core was finely ground and packed evenly into a 4-mm zirconia rotor and sealed at the open end with a Vespel cap. The rotor was the spun at 14 kHz on a Bruker Ultrashield 400.13 WB Plus with a 9.2 T magnet operating at 79.495 MHz for ^{29}Si and a dwell time of 10 μs, 2048 acquisitions were obtained in all cases. In order to obtain quantitative data a recycle delay of 30 s was used, which allowed for full relaxation of the signal. The magic angle was set to 54.734°, using KBr as a reference. The quantitative information on the fractions of silicon ions present in silicate tetrahedra with different connectivities was obtained by deconvolution of the single-pulse spectrum. In this work, the spectrum was fitted by the iterative fitting of the hydrate peaks to Voigt lineshapes using IgorPro 6.35A5 (Wavemetrics, Inc., U.S.A.).

2.5. Transmission Electron Microscope (TEM)

Fine powders were scraped from the core of the cylinder, and suspended with ethanol. The suspension was then deposited on a carbon film and air-dried for 5 min. Ten-nanometer-diameter gold particles, coated the carbon film to assure proper alignment of the reconstruction. A Titan CT TEM, equipped with *Xplore3D* tomography software was used. To ensure that no $Ca(OH)_2$ (CH) particles exist, which will cause strong scattering, the diffraction pattern was investigated before the tomography measurement was conducted. The rotation range was set as 0° to −65° and 0° to +65°, which collected 361 projection images that were then aligned using IMOD software [18].

2.6. Scanning Transmission X-ray Microscope (STXM)

Fine powders extracted from the core of the cylinder were suspended in distilled water, and then a 0.02 μl drop was transferred onto a 100 nm thick silicon nitride window. The window was then attached to a thin steel plate and fixed to the STXM sample stage. As shown in Fig. 1, the incidence X-ray beam can be tuned to continuously changing energy values, and the sample stage allows scanning at high spatial resolution; therefore X-ray Absorption Spectra (XAS) can be recorded at specific locations of interest, providing point analysis. By applying a high resolution Fresnel zone plate, the spatial resolution of STXM can reach 25 nm. To study the chemical environmental evolution, a control sample of pure C_3S, w/c = 5.0 with a curing age of 1.5 years, was also studied. The high w/c ratio of the sample was necessary to enable the study of an isolated cement particle under STXM. This would not be possible with a standard w/c ratio, as the particles would clump, resulting in a thick sample, which X-ray could not penetrate. Throughout this study the 50-year-old sample tested by STXM will be referred as C_3S50 and the 1.5-year-old sample will be referred as $C_3S1.5$.

The STXM apparatus is affiliated to Advanced Light Source (ALS) at Lawrence Berkeley National Laboratory (LBNL) at beamlines 5.3.2.1 and 5.3.2.2, with energy scanning ranges of 700–2200 eV and 250–800 eV, respectively. X-ray absorption spectrum typically records the absorption intensity versus the incident beam energy. An absorption edge is encountered when the incident beam energy

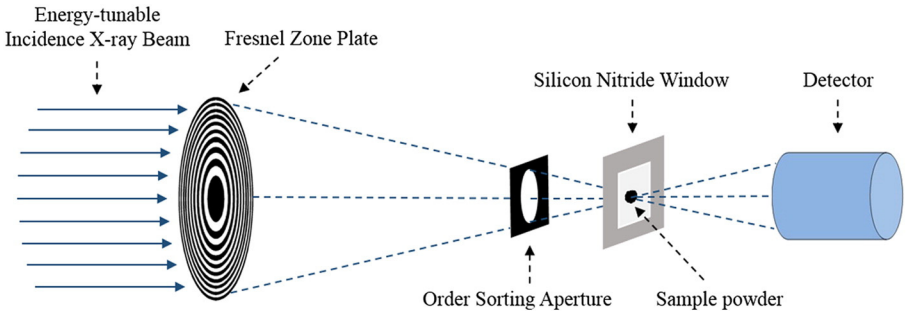

Fig. 1. Schematic diagram of STXM.

is close to the specific energy difference between the inner-shell and outer-shell orbitals in a certain atom, when significant absorption is observed due to the excitation of inner-shell electrons to empty outer-shell orbits. This study focused on a unique part of the X-ray absorption spectra, from about 30 eV before the absorption edge, to 30 eV after the edge, resulting in a whole energy extension of about 60 eV. This unique part is named Near Edge X-ray Absorption Fine Structure, shortened as NEXAFS. Specifically, the NEXAFS spectra of calcium (Ca) $L_{3,2}$-edge, silicon (Si) K-edge and carbon (C) K-edge were studied. They correspond respectively to the excitation of L-shell electrons in Ca atoms, K-shell electron in Si atoms and K-shell electron in C atoms. The NEXAFS spectra are sensitive to the coordination status of the studied atom. Peak-position shift or curve shape changing would be observed when varying atomic environment. The energy resolution can be as high as 0.1–0.2 eV. Alteration in the chemical environment of Ca and Si will affect their NEXAFS, providing the opportunity to obtain valuable chemical information, e.g. the coordination state or the changes in the neighboring atoms in molecular structure [19,20]. NEXAFS spectra at carbon K-edge could yield the information of carbonation [34].

STXM data can be collected in several ways: a) Image can be generated from the absorption data of each pixel. In this case, the beam energy is fixed and the scanning is only conducted in spatial dimension. Usually the data is converted to optical density (OD) image through the Beer–Lambert law: $OD = -\ln[I / I_0]$, where I is the intensity of the transmitted beam and I_0 is the incidence beam intensity [21]. A bright area on the OD image indicates a large absorption. Note that the amount of absorption is affected to by three factors: density, thickness and the absorption coefficient. Specially, the absorption coefficient can be largely increased to a significant degree when the incident beam energy reaches the absorption edge of certain elements, as explained earlier; b) line scan data can be obtained by scanning both the incident beam energy (within the range of about 60 eV and centered at the absorption edge) and spatial dimension along a straight line on the sample. Line-scan data contains the NEXAFS spectra of each pixel on that line; c) Stack scan is the most complete scan mode and can measure the NEXAFS on each pixel over the whole image. *AXis2000 software* is used to process all types of data [22].

3. Results

3.1. XRD

In the XRD shown in Fig. 2, for both CP and SP, three phases can be identified, $Ca(OH)_2$ (CH), C_3S and C–S–H. Unsurprisingly, CH is the most dominant phase in both plots, since this is the major crystalline hydration product. As would be expected due to its lack of crystallinity, the C–S–H phase exhibits no sharp peaks on the plots. Instead, a broad peak from 33° to 38° can be assigned to the C–S–H structure. A corresponding spacing of 2.7 to 3.1 Å confirms the poorly crystallized nature of C–S–H in hardened C_3S paste. Similarly broad peaks were observed by Bergold [23], where the C–S–H (alite paste at 23 °C with w/s = 0.5 after 65 h of hydration) peak values are almost identical with those reported herein.

A small peak at $2\theta = 59°$ is assigned to C_3S [23,24]. The intensity is significantly low so that hydration degree can be concluded to near 100%. Note that there are no peaks that can be assigned to $CaCO_3$. It can be claimed that no crystalline carbonate forms even after 50 years; this is also supported by the results of the NMR and STXM study, discussed below. In summary, the XRD study proves that, over the span of 50 years almost complete hydration has occurred with zero carbonate crystals. The C–S–H remains poorly crystalline as at the very early age.

3.2. SEM

Usually under the secondary electron (SE) mode, different components, such as unreacted C_3S, Ip C–S–H and Op C–S–H, are less distinguishable. Only under the back scattered electron (BSE) mode can they be identified by grayscale value. However, in this 50-year-old C_3S paste sample, SE images show unique features that allow identification of different components (Fig. 3).

The SEM results support those indicated by XRD data, in that the sample contains almost no unreacted C_3S and no $CaCO_3$. As shown in Fig. 3, three features are exposed on the fractural surface: 1) interlaced fibers that form the matrix; 2) globular core with rough surfaces, surrounded by a fibrillar matrix; and 3) a crystalline phase in plate-shape. These are identified as Op C–S–H, Ip C–S–H and CH respectively. The reasoning is as follows: The fibrillar material distributed throughout the whole matrix is oriented in a radial fashion outside the globular core. The thickness of the fibers is approximately 150–250 nm (most fibers are of uniform thickness). Recall that in the early age hydration fibrillar Op roots on the boundary between Ip and Op C–S–H, in a radial format [14]. When the Op of adjacent C_3S particles interlaces with each other, the mixture sets and begins to gain strength. Therefore, the universally existing fibrillar material in the 50-year-old sample most probably comes from the early age fibrillar Op. Because the XRD results determined that the amount of unreacted C_3S is negligible, the globular core must be the inner product, containing, most likely, very small amount of C_3S. Lastly, being the only crystalline phase in the sample, CH must account for the large plates in the images, whose smooth surface and sharp edge strongly indicate crystalline morphology.

The EDS data were collected at various locations, as shown in Table 1 (the names of these locations are assigned according to the above analysis). The Ca/Si ratio of Ip and Op C–S–H is consistent with other studies [25]. Reported Ca/Si ratio of C–S–H in pure C_3S paste is ~1.7, which is about the same as that of Ip C–S–H (~1.68), but smaller than that of Op C–S–H (~2.02) in this study. The observed Ca/Si ratio in Op C–S–H indicates a higher Ca–OH bond content in the Op zone. These bonds are either in solid solution state inside C–S–H (as suggested by Richardson [10]) or have formed nanoscale fine crystalline CH which is too small to be distinguished from C–S–H.

Many researchers have suggested that the Ip is more likely to form in an in-situ reaction pattern, i.e. product forms where reactant is.

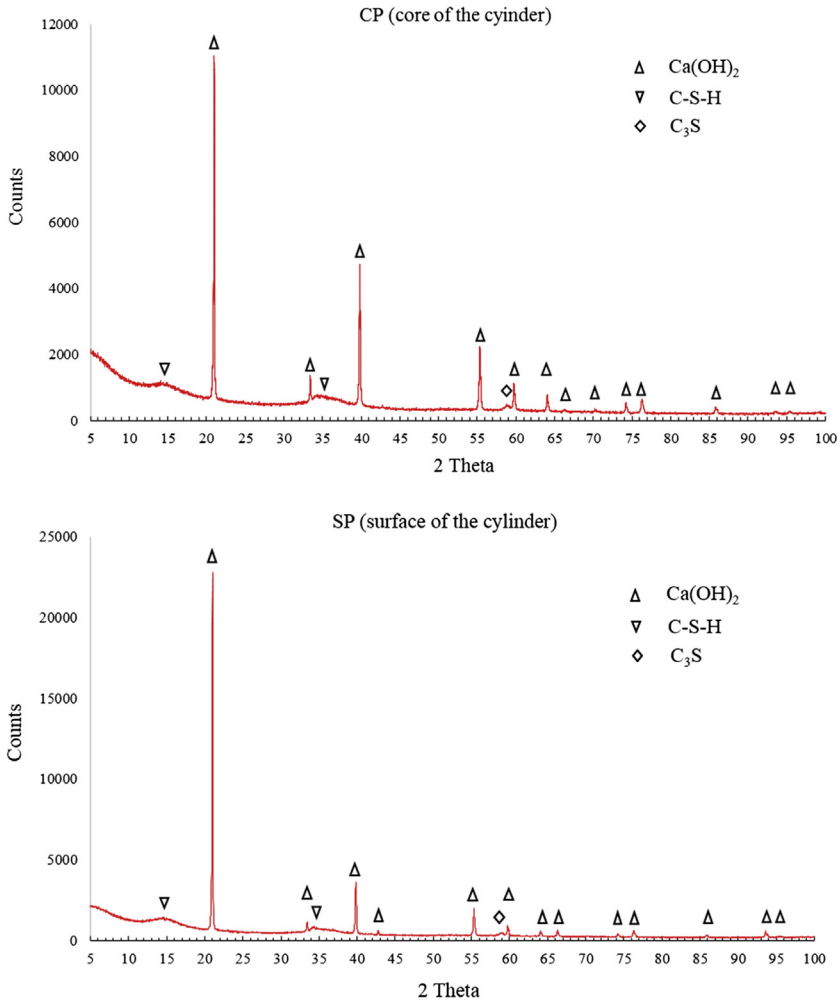

Fig. 2. XRD results of CP (core of the cylinder) and SP (surface of the cylinder).

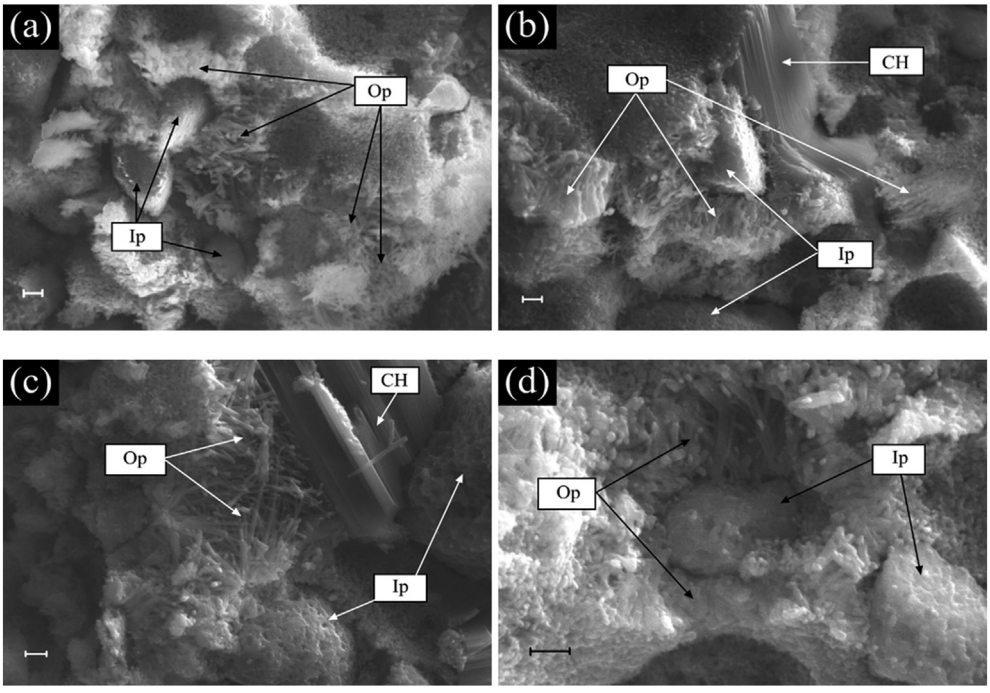

Fig. 3. Secondary Electron images on different locations in CP (core of the cylinder), bar length 1 μm.

Table 1
Statistics of EDS data of the 50-year-old C_3S paste.

Phases	# of testing points	Average atomic Ca/Si	Standard deviation
Ip C–S–H	11	1.68	0.15
Op C–S–H	6	2.02	0.15
CH	3	14.12	2.41

However, the Ca/Si ratio (~1.68) of Op C–S–H is much smaller than that of the original C_3S. This suggests that, although the Ip is denser than Op [11,12], Ca^{2+} ions are efficient in migrating to the Op zone. It is worth mentioning that EDS under the SE model is more qualitative than quantitative, due to the shadowing effect of uneven surface. Besides, the signal comes from 0 to 3 μm beneath the surface, while the material of interests could be only 1 μm thick [26]. But considering the standard deviation, the tendency is reliable as a comparison within this study and other published SEM–EDS results.

3.3. TEM

In conducting the TEM measurement, great care was taken in order to find a particle that contained both Ip and Op C–S–H but no CH. The crystal structure of CH would greatly affect tomographic collection and introduce artifacts. Images of particles at various rotation angles are shown in Fig. 4 in series from (a) to (f). Projection images from the 3D acquisition are provided here instead of the 3D reconstruction, because there was no single complete data set collected from −65° to 65°, without beam damage or the gain moving from view. As a result the missing wedge of the sample largely decreases the resolution of the 3D reconstruction, and therefore in this case 2D images are better in showing details. As the sample rotates from (a) to (f), one part (area P) of the particle disappears and the other (area Q) appears. We conclude that the observed particle is a conjunction of Op C–S–H (area P) and Ip C–S–H (area Q) with a total dimension of about 150 nm. White arrows in Fig. 4(b) mark the boundary between Ip and Op C–S–H. The rationale is explained as follows.

The determination of Ip and Op C–S–H in the image series is based on the TEM morphological observation of C_3S pastes obtained from the literature [10,14,27]. The Op C–S–H of hydrated neat C_3S grain is reported to be composed of long-thin particles, very similar to the features of area P in this TEM results. Although it can alter to foil-like Op C–S–H when the hydration environment is rich in Al^{3+} (for instance in the case of alkali activation/Slag addition [10]), the Op C–S–H in pure C_3S paste (and in also C_2S paste [10]) is fibrillar all through the hydration process. The diameter seems to grow from several tens of nanometers at very early age to about 100 nm at eight years old, and eventually to ~200 nm at 50-years-old, as indicated by the SEM results in this work.

At a finer scale (<10 nm), the Op C–S–H fibers are composed of large numbers of long thin particles aligned along its length. The particles are about 1.5–2 nm in their smallest dimension and can be a few nanometers to many tens of nanometers long. Adjacent particles are separated by a transparent layer of about 1.5 nm thick, which is most likely to be water layers when the sample is in moisture [8]. Based on these observations, area P is considered to be Op C–S–H because of its alternating lamellar structure of long-thin particles and water layer. The thickness of the particle (1.5-2 nm) is in good agreement with Richardson's work on C_3S pastes [10].

Area Q has similar morphology as the Ip C–S–H reported in other studies [10,27]. Unlike the fibrillar Op C–S–H, the Ip C–S–H appears to be the aggregation of globular particles. This results in a denser packing than Op. Besides, the texture of Ip is rather homogenous, while that of Op is with a preferred growing direction.

3.4. NMR

To determine the silicon anion structure present in the C–S–H phases, ^{29}Si MAS NMR was used to obtain quantitative information of the fraction of silicon present in different tetrahedral environments. The original spectrum shown in Fig. 5 has only two resolvable peaks at shifts of −79.0 and −85.1 ppm. Anhydrous C_3S contains nine distinctive silicate anion environments, which are represented in a spectrum as five resolvable peaks in the range of around −68 to −75 ppm [28]. As there is no indication of any peaks in this range, it can be concluded that the C_3S was fully reacted, which is in agreement with the results obtained from the XRD. Because the spectrum has zero intensity in the range of −89 to −103 ppm there are no Si anions in either chain branching sites or three dimensional frameworks (Q^3 or Q^4) that form when pastes carbonate [29], confirming that the C–S–H has not been carbonated, which is also in agreement with XRD results.

From integration of the areas under each deconvoluted peak, it is possible to calculate the percentage of Si atoms in each environment, and compare this with a sample of C_3S over a range of hydration length from 12 h to 26 years [9]. The results obtained from that study are given

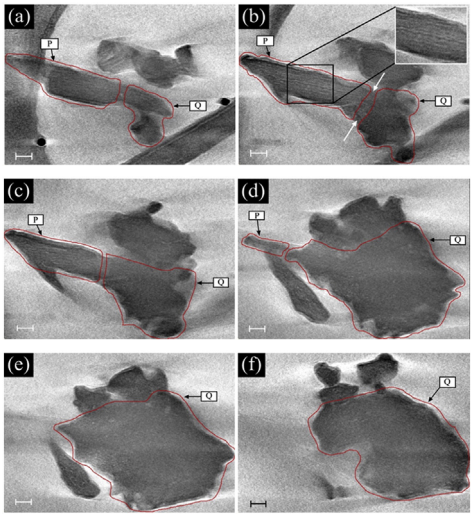

Fig. 4. A series of slices from the reconstruction of a particle in C_3S paste, which is unidirectionally rotated from (a) to (f); bar length is 20 nm. Areas P and Q are, respectively Op and Ip C–S–H respectively. During rotation the feature of area Q increases while that of area P fades.

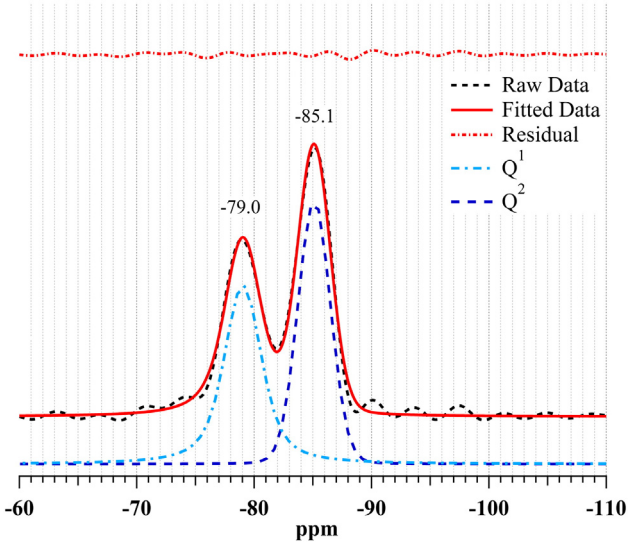

Fig. 5. ^{29}Si NMR spectrum of 50-year-old C_3S paste, deconvoluted to Q^1 (−79.0) and Q^2 (−85.1). All y-axes are set to the same intensity.

in Table 2 with the additions of the Mean Si tetrahedron Chain Length (MCL). The 50-year-old sample was cured in saturated limewater for three years and then sealed in a plastic bottle. After half-century hydration, the MCL is only 4.18, compared with 2 at 12 h and 3.27 at 1 year [9]. The polymerization process is so slow, that one can expect within the normal service life time (50 years to 1 century) that C–S–H in C_3S hydration product would always have a low degree of polymerization.

The results in Table 2 suggest that dimers are formed first from monomers (Q^0), then longer chains can be formed (Q^2) from the linking of dimers with monomers, but chains longer than dimers do not form directly from monomers alone. This is verified by the work of Lippmaa et al., who reported a reduction but not a complete halt in monomer consumption and Q^1 production during the formation of Q^2 units [28]. If Q^2 units were formed directly from monomers, the consumption of monomers would most likely increase, as more units are needed in chains than in dimers. The results in the table also show that significant quantities of Q^2 units are not formed until a minimal amount of monomers remain. As Lippmaa et al. found Q^1 production declines with initial Q^2 production; there is the indication that regardless of the degree of hydration of the paste, C_3S systems are not able to form both dimers and longer chain simultaneously.

The formation of Q^2 units does not start until over 30% of anions are present as dimers, once this has occurred the percentage of dimers present never falls below 40%, even after 40 years; see Taylor et al. [30]. As the method of polymerization is that of linking dimers and monomers, the most likely reason for the discontinuation of dimer consumption in order to form longer chains is the absence of any monomer species at this stage. If this is the case, it would also indicate that dimers cannot link with each other and as such the sequence of chain lengths is possible $(3n-1)$. As observed by TEM, the fine particles in Op C–S–H can be as long as several tens of nanometers, much longer than the MCL (4.18 SiO_4^{4-} tetrahedrons, which is about 1.1 nm [31]). There is a missing link from this short SiO_4^{4-} tetrahedron chain to the long-thin particle. According to Richardson [10,32], this can be explained by Ca^{2+} replacing the bridging SiO_4^{4-} tetrahedron in the regular tobermorite structure, or the protonation of oxygen atom that decreases the length of the Si chain. This model explains the phenomena (such as MCL and Ca/Si) but it has been difficult to prove experimentally. The STXM results discussed below provide some new evidence.

3.5. STXM

NEXAFS (Near Edge X-ray Absorption Fine Structure) provides abundant information about the bonding and coordination state of absorbing atoms and STXM allows in-situ NEXAFS study at local area of solid material [33]. Multiple factors can affect the fine structure of absorption spectra. Absorption peaks can either be assigned to the excitation of inner-shell electrons to outer-shell energy levels, or the multi-scattering process of photon–electron interaction. These fine structures are sensitive to oxidation status and coordination symmetry.

Table 2
Quantity of Si anions in each environment as a percentage obtained from integration of the peak areas.
Data from 12 h to 26 years are from Rodger [9].

Age	Q^0	Q^1	Q^2	MCL
12 h	89	11.0	0.0	2.00
1 day	68	30.0	2.0	2.13
7 days	48	43.0	9.0	2.42
14 days	33	52.0	15.0	2.58
1 month	30	53.0	17.0	2.64
3 months	18	62.0	20.0	2.65
6 months	14	65.0	21.0	2.65
1 year	10	55.0	35.0	3.27
2 years	6	52.0	42.0	3.62
26 years	0	42.0	58.0	4.76
50 years	0	47.9	52.1	4.18

For example when the degree of polymerization increases, the major peak in Si K-edge increases also. In Ca $L_{3,2}$-edge, when the ca coordination is in tetrahedral, octahedral or cubic symmetry, a split in major-absorption peaks can be observed. The difference in the intensity ratio among the peaks can provide qualitative information on the degree of structural distortion. In the research reported here, the results of NEXAFS of Ca $L_{3,2}$-edge, Si K-edge and C K-edge of the 50-year-old hydrated C_3S sample (C_3S50) were studied; a 1.5 year C_3S paste ($C_3S1.5$) was also studied for comparison.

Ca $L_{3,2}$-edge

STXM results of Ca $L_{3,2}$-edge are shown in Fig. 6. Stack data were collected from both areas: (a) C_3S50 and (b) $C_3S1.5$. As described in previous section, stack data contain the NEXAFS information of each pixel in the field of view. By comparing the spectra of different areas, one can distinguish between various components. The hydrated particles in Fig. 6a were not damaged during sample preparation, enabling in-situ observation. Through investigating the NEXAFS spectra of each pixels of the whole image, two representative spectra were extracted, as shown in Fig. 6c. One was collected from site 1, a margin area of a particle in Fig. 6a, and the other from site 2 on a bulk particle. In Fig. 6b, two representative spectra were also extracted, after examining spectra of each local area in the field of view.

The Ca $L_{3,2}$-absorption edge spectra correspond to the excitation from Ca 2p to 3d orbitals. Two major peaks (X1 and Y1) can always be observed due to of the loss of degeneracy of 2p orbitals by spin–orbital interaction [36]. Despite the chemical status of Ca, these two major peaks are observed in the $L_{3,2}$-edge spectra of Ca-containing minerals. The symmetry of the CaO_x coordination complex could further break the degeneracy of states, resulting in two minor peaks to the left of major ones. This phenomenon was well explained by crystal field theory, which was later combined with molecular orbital theory and developed to ligand field theory [36]. In case of perfect octahedral symmetry, two major peaks are strongly split so that the intensities of the minor peaks are comparable to those of the major peaks. Besides, the energy differences between major and minor peaks are also significant. These two characters can be used to indicate the strength of the crystal field of the CaO_x complex.

Table 3 classifies the Ca coordination status into two categories based on the coordination symmetry. When the coordination is in octahedral symmetry (or near octahedral symmetry), such as the case of CH, calcite and dolomite, the spectra will be strongly affected by the "crystal field" effect. Significant splitting in major peaks X1 and Y1 is allowed, and strong minor peaks X2 and Y2 could be observed in this case. The energy difference between adjacent major and minor peaks is 1.2–1.4 eV. Spectrum of CH is shown in Fig. 6c; spectra of calcite and dolomite can be found in [36,37]. Meanwhile in aragonite and gypsum, the coordination symmetry of Ca is rather irregular, which is considered to be a "weak crystal field". In this case, 3d orbital is less degenerated and minor peaks (X2 and Y2) change in two ways: they decrease in intensity, and they shift to higher energy. This makes the minor peaks less distinguishable on the NEXAFS spectra, as well as shortens the distance between major and minor peaks. This observation, verified by study of many minerals, can therefore be applied to the interpretation of Ca coordination status in C–S–H and CH.

C–S–H and CH are the two main hydration products. Ca in CH is in perfect octahedral symmetry and a strong splitting is observed in its $L_{3,2}$-edge spectra, as shown in Fig. 6c. Energy difference between major and adjacent minor peaks is ~1.4 eV. $L_{3,2}$-edge spectra of C–S–H were also reported in earlier literatures [15,35], which exhibited weak splitting. In Fig. 6, spectra of site 1 in both samples exhibit weak splitting, with an energy difference between major and minor peaks of 0.9–1.1 eV, while energy differences on spectra of site 2 in both samples are ~1.3 eV. Therefore we assign site 1 to the C–S–H-rich region and site 2 to the CH-rich region. Also from a morphological point of view, site 1

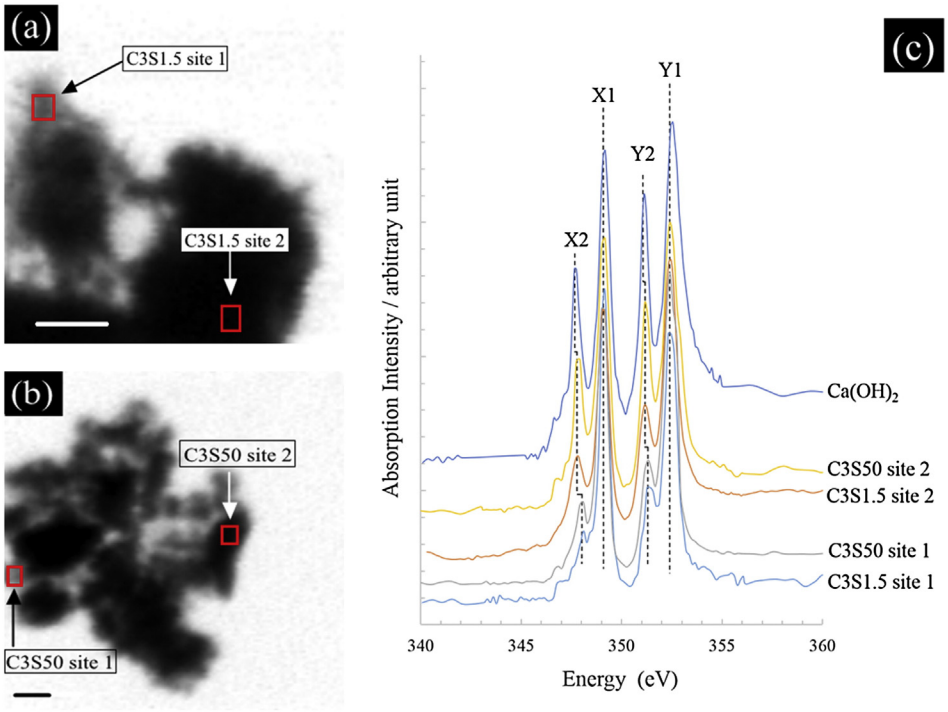

Fig. 6. Ca $L_{3,2}$-edge, scale bar length 500 nm: absorption image of (a) $C_3S1.5$ and (b) C_3S50; (c) NEXAFS spectra of hydrated C_3S samples, compared with that of pure CH. Spectrum of CH is from [44].

in Fig. 6a locates on fibrillar margin area of hydrated particle, resembling the morphology of Op C–S–H. In Fig. 6b, not much morphological information is evident, since the grinding process largely altered the microstructure.

The small energy difference and the low intensity of minor peaks, of C–S–H in both C_3S50 and $C_3S1.5$, are similar with the spectra of aragonite and gypsum, as shown in Table 3. The relative weak crystal field effect in C–S–H indicates poor symmetry of Ca coordination structure. Spectra of Ca in CH of both samples share the same feature with spectra of pure CH, as well as calcite and dolomite [36]. It's worth pointing out that the major peaks X2 and Y2 are consistent among all spectra.

Table 3
Peak characters from the Ca L-edge spectra, some data are from [36,37].

Compound	ΔX/eV	ΔY/eV	Symmetry of coordination
Pure CH	1.4	1.4	Octahedral
CH in C_3S50 (site 2)	1.3	1.3	
CH in $C_3S1.5$ (site 2)	1.3	1.3	
Calcite	1.2	1.3	
Dolomite	1.3	1.3	
Aragonite	0.8	0.8	Irregular
Gypsum	0.9	0.9	Irregular
C–S–H in C_3S50 (site 1)	0.9	1.1	Unknown
C–S–H in $C_3S1.5$ (site 1)	1.0	0.9	

Changing of chemical environment seems to be solely indexed by intensity and energy values of minor peaks.

Si K-edge

STXM results at Si K-edge are shown in Fig. 7. Si K-edge has a higher absorption energy (compared to Ca $L_{3,2}$-edge) and therefore ensures greater penetration depth, resulting in more morphological details in the absorption images. In $C_3S1.5$ (Fig. 7(a) and (b)), fibrillar Op C–S–H covers the surface of C_3S particles, while the core area appears to be featureless. In C_3S50 ((c) and (d)), the morphology is not well retained after sample preparation.

Absorption at Si K-edge has only a single absorption edge with no splitting. A designation of the major peak as X and the minor peak as Y in Fig. 7e is given. The major peak is due to excitation from 1s orbital to 3p orbital and minor peaks are due to multi-scattering phenomena [38,39]. Both peaks shift to higher energy along with the hydration process. Li et al. [38] reported that major peak X shifts to higher energy when the degree of polymerization increases, which is in good agreement with the results of this study. Peak X of C–S–H gel in the 1.5-year-old sample locates at 1848.1 eV, 0.4 eV higher than that of anhydrous C_3S. At 50 years, it changes to 1848.3 eV. As the degree of polymerization increases, the energy level of Si 1s orbital decreases, which increases the excitation energy. Note that the change is not significant, suggesting that Si is always in 4-fold tetrahedron coordination in the C_3S hydration system.

The minor peak Y increases with hydration at a higher rate compared to that of peak X, so that the energy difference, ΔE, between peaks X and Y increases. As shown in Table 4, the hydration reaction increases ΔE from 11.2 eV (C_3S) up to 12.8–13.0 eV (1.5-year-old), and eventually to 16.5 eV at later age (50-year-old), indicating significant alternation in multi-scattering behavior around Si atoms. According to the NMR study, the MCL is about 4.2 at 50 years, compared with ~3.5 at 1.5 years. The multi-scattering phenomenon is affected by the closest several neighboring atoms, and seems fairly sensitive to the degree of polymerization. An increase in the MCL by 0.7 results in an increase in the ΔE by 3.5 eV. It is not fully understood how the atomic

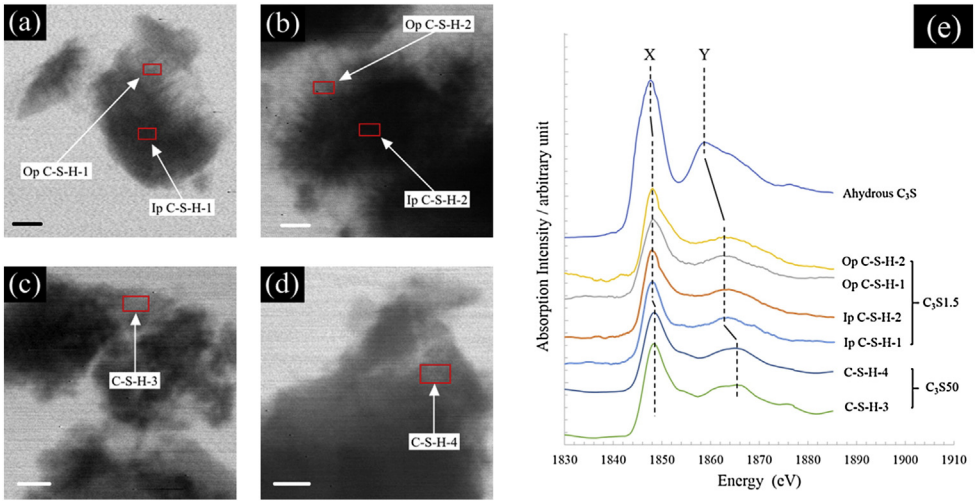

Fig. 7. Si K-edge, scale bar length 1 μm: (a) (b) absorption image of $C_3S1.5$; (c) (d) absorption image of C_3S50; (e) NEXAFS spectra of marked areas.

structure changes the multi-scattering behavior. More work is worth doing if this proportional relationship holds for various hydration ages of C–S–H. Future research will focus on the multi-scattering behavior, and how it is related to the atomic structure, especially the SiO_4^{4-} linkage of C–S–H.

C K-edge

To complement the carbonation study of C_3S50, the NEXAFS spectra of Carbon at K-edge were investigated, as shown in Fig. 8(a). A line scan was conducted crossing the border of a gel cluster, as marked by the red arrow. The absorption spectrum of each pixel on the arrow was recorded by line scan. Spectra of a thin area at location *b* and a slightly thicker area at location *a* were shown in Fig. 8(b). If the samples were significantly carbonated, two distinguishable peaks would be expected near 285.0 eV and 290.0 eV [34]. On the contrary, the spectra of both locations *a* and *b* exhibit no obvious peak near 285.0 eV and only a weak peak at 290.2 eV, whose intensity is of the same order as the noise of the spectra. Compared with the unambiguous peaks of carbonated C–S–H gel [34], it could be concluded that the sample contains a negligible amount of carbon, in agreement with NMR and XRD.

4. Discussion

Both XRD and NMR studies indicate that the 50-year-old paste has not been altered by carbonation. No peak seen on either the diffraction spectra or the ^{29}Si NMR spectrum can be assigned to $CaCO_3$. From the chemical composition point of view, the sample is merely a mixture of C–S–H, CH with a negligible amount of unreacted C_3S. NEXAFS spectra of carbon K-edge support this conclusion, as no specific absorption of carbon atom was observed.

In the XRD results, only one broad peak is assigned to C–S–H in this study. Compared with previous research on calcium silicate hydrate crystals [32] and synthesized C–S–H (I) [8], the hydration products (both Ip and Op) remain disordered along all three-crystal axes, even after 50 years of curing. Meanwhile the MCL remains below 5, despite almost full hydration. This indicates that at ambient temperature and pressure, the poorly crystalline nature of C–S–H gel almost remains unchanged throughout concrete's typical service life.

Many researchers have discussed atomic models of C–S–H gel, most starting with the structures of tobermorite or jennite [32]. The amorphous nature is accounted by the omission of bridging tetrahedrons and the variation of interlayer Ca and water content. Numerous work were conducted on crystallography and Si linkage, yet very few study on the chemical environment of Ca has been reported. In this study, an important clue was found in the NEXAFS spectra.

As shown in Fig. 6 and Table 3, C–S–H falls into the category of aragonite and gypsum, where the coordination structure of Ca is in poor symmetry. As shown in Fig. 9, the coordination structure of Ca is 7-fold in tobermorite and 6-fold in jennite Fig. 9. The latter has an octahedral symmetry, as is found for Ca in CH and calcite. If the modeling of C–S–H gel starts with jennite, it should be expected that its NEXAFS spectrum is analogous to CH and calcite. The NEXAFS spectra of Al-tobermorite were validated by Jackson et al. [16], exhibiting minor peaks that are less intensive and less distinguishable. NEXAFS spectra of both 1.5 years and 50 years old C-S-H have weak minor peaks, indicating strongly a non-octahedral coordination symmetry of Ca atoms. Therefore, the Ca coordination in the atomic structure of C–S–H in this study can be better described by a tobermorite structure rather than jennite structure. This is the first time NEXAFS spectra are applied to demonstrating that at the atomic scale C–S–H resembles more of a tobermorite structure where Ca atom has irregularity in its symmetry. As reported herein, this is important evidence unraveling the structural information of C–S–H, since the relation between coordination symmetry and NEXAFS has been proved by both theory and experimental results of many other minerals [20,36,37].

The tobermorite model has a limitation in explaining the Ca/Si ratio of C–S–H. Richardson [10] demonstrated in his model that the Ca/Si ratio of tobermorite can be largely increased by a variation in the degree of protonation or by Ca replacing the bridging SiO_4^{4-}-tetrahedron. These bridging Ca ions also contribute to NEXAFS spectra; therefore they must also be in poorly symmetric coordination, for example the 7-fold irregular symmetry as seen in the intralayer Ca sheets in tobermorite (Fig. 10). Due to the same reason, the "tobermorite–$Ca(OH)_2$ solid solution" model seems questionable, since the octahedral coordinated Ca atoms in $Ca(OH)_2$ would yield a strong peak-splitting, which is not the case for C–S–H.

Table 4
Energy difference, ΔE, between minor and major peak at Si K-edge.

	Sample	X (eV)	Y (eV)	ΔE (eV)	Hydration time (years)
	C_3S	1847.7	1858.9	11.2	0
	Ip C–S–H-1	1848.1	1860.9	12.8	1.5
$C_3S1.5$	Ip C–S–H-2	1848.1	1860.9	12.8	1.5
	Op C–S–H-1	1848.1	1861.1	13.0	1.5
	Op C–S–H-2	1848.1	1861.1	13.0	1.5
C_3S50	C–S–H-3	1848.3	1864.8	16.5	50
	C–S–H-4	1848.3	1864.8	16.5	50

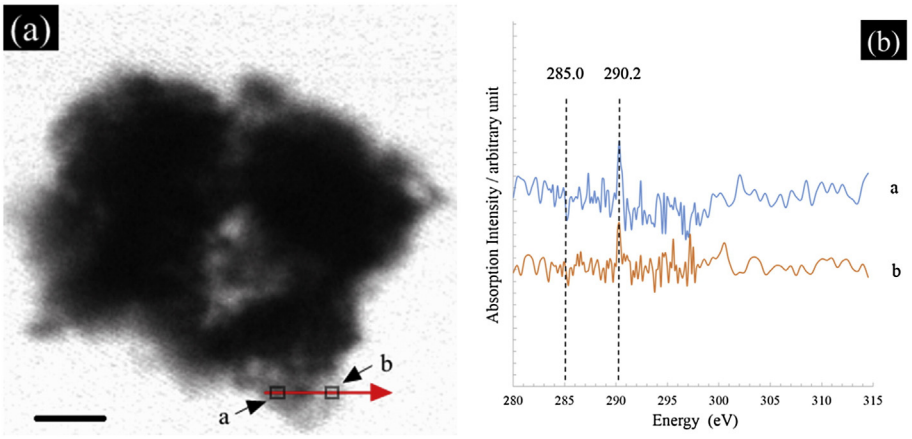

Fig. 8. C K-edge, scale bar length 1 μm: (a) absorption image, red arrow indicates the route of line scan; (b) NEXAFS spectra of locations *a* and *b* on the scan route. (For interpretation of the references to color in this figure legend, the reader is referred to the web version of this article.)

Previous research results using SAXS (small angle x-ray scattering) and SANS (small angle neutron scattering) [42,43] strongly indicate that there exists two successive levels of organization in C–S–H gel (Ip and Op) of OPC. At the atomic level (<5 nm), disordered Si chains, Ca sheets and water layers form nano-particles. Jennings [11] claims this particle to be a globular particle of about 5 nm. In contrast, Richardson's results [10] indicate it to be long thin fibers of 2.5–3.5 nm thick and tens of nanometers long. It should be clarified that Richardson's observations quoted here focus on the fibrillar Op C–S–H of pure C_3S paste, while Jennings' results are based on homogenized information of various types of C–S–H paste. Despite the shape of the particles, they are the "building blocks" of C–S–H. At a coarse level (5–200 nm), the fine particles form the microstructure of C–S–H. Using pure C_3S paste as an example, the Op C–S–H fibers are formed by the alignment of the long-thin particles along their longitudinal direction. The featureless microstructure of Op C–S–H in C_3S paste can be described by the packing of globular particles (several nanometers large). Considering the fact that the C_3S in this study comes from a different source compared to Richardson's work, and that the age is also different, it can be concluded that these long-thin particles are naturally the basic building blocks of fibrillar Op C–S–H in C_3S paste. The dimension of these particles and the way they are aligned do not change during the hydration process. The thickening of the Op C–S–H fibers is accomplished by more long-thin particles aligning on the fiber, rather than thickening of the particles. However, these particles can alter significantly when the contents of Ca^{2+} and Al^{3+} increase in the reaction system. Increasing amounts of mineral admixture (fly ash, slag, natural pozzolan, silica fume, and so on) are now used as supplementary cementitious material. It is thus critical to understand the mechanism of how SiO_4^{4-} tetrahedron and Ca^{2+} form the fine particles and why these particles keep a constant size during the hydration, and the mechanism of how the addition of Ca^{2+} and Al^{3+} favors the formation of globular particles rather than long-thin particles in pure C_3S paste. As the dominant binding material, the formation of C–S–H is extremely important. Understanding the above mechanisms can enlighten the development of high-efficiency chemical/mineral admixture and design of high-performance concrete.

5. Conclusions

A multi-scale analysis was conducted that compared the structure of a late-age C_3S paste to similar paste at earlier age. No evidence of carbonation was observed in the 50-year-old sample; unreacted C_3S was also rare. The atomic structure of the late-age C–S–H gel can be described as repeated units of SiO_4^{4-} tetrahedron, CaO_x polyhedron and H_2O molecules. Even after 50 years of hydration, the structure was still ordered only at short length. The coordination state of Ca^{2+} has irregular symmetry, rather than octahedral symmetry. Since Ca^{2+} in tobermorite shows 7-fold irregular symmetry compared to jennite that has an octahedral symmetry, the short-range atomic scale of the samples is more an analogy to that of tobermorite rather than jennite. The MCL increased along with the degree of hydration, from ~3.5 at 1.5 years to 4.18 at 50 years. It is possible that the bridging SiO_4^{4-} tetrahedron is replaced by bridging Ca^{2+} at multi-locations, which explains both the short chain length and Ca/Si ratio. The bridging Ca^{2+} is also in non-octahedral symmetry, as indicated by Ca $L_{3,2}$-edge NEXAFS. In Si K-edge, major peak shifts to higher energy with increasing MCL, and so does the minor peak. The energy gap between major and minor peaks in Si K-edge seems to be

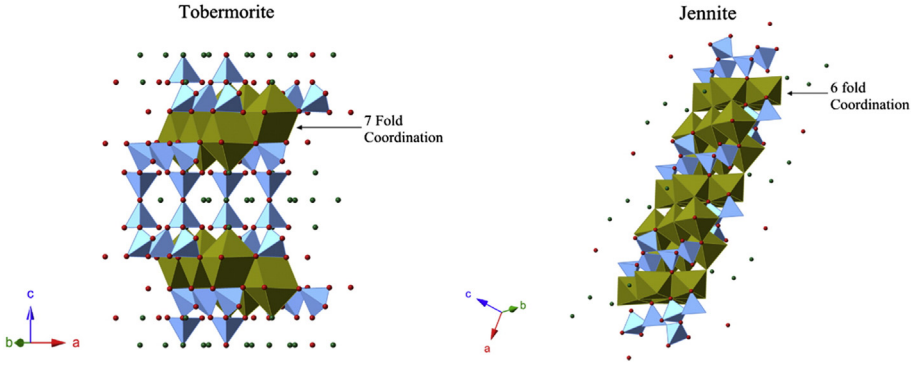

Fig. 9. Atomic structure of 11 Å-tobermorite and jennite [40,41].

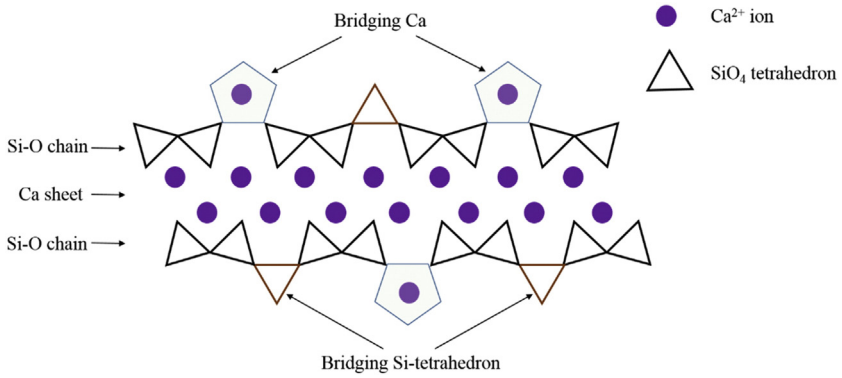

Fig. 10. Scheme of short chain in tobermorite-based C–S–H.

proportional to the MCL, and therefore could be an indicator of degree of polymerization.

At the nano-scale, Ip C–S–H is featureless and seems to be the flocculation of globular particles. In contrast, Op C–S–H showed clear radial growing fashion, rooting on the surface of the Ip–Op boundary. Thickness of Op C–S–H fibers increases along with hydration, from several tens of nanometers, to ~100 nm at 8 years and eventually to ~200 nm at 50 years. The fiber was composed, at a finer scale, of thin fibrillar particles (1.5–2 nm thick and several tens of nanometers long). These particles are the basic building blocks of Op fibers and tend to align along the longitudinal direction. Between the fibrillar particles there exist layers of empty space with thickness of about 1.5 nm, which could be filled with water before sample was dried out. Considering such a narrow space, they are most probably physically absorbed water. The growth of Op fibers is accomplished by more particles aligned on the fibers, instead of the thickening of the particles themselves.

Acknowledgments

Guoqing GENG's study and research in UC Berkeley are supported by the China Scholarship Council (file No. 201206090127). The authors thank Timothy Teague for the technical help with the SEM and XRD experiments. This research is funded by the National Research Foundation-Prime Minister's office, Republic of Singapore through a grant to the Berkeley Education Alliance for Research in Singapore (BEARS) for the Singapore–Berkeley Building Efficiency and Sustainability in the Tropics (SinBerBEST) Program. BEARS has been established by the University of California, Berkeley as a center for intellectual excellence in research and education in Singapore. The Advanced Light Source is supported by the Director, Office of Science, Office of Basic Energy Sciences, of the U.S. Department of Energy under Contract No. DE-AC02-05CH11231.

References

[1] P.K. Mehta, P.J. Monteiro, Concrete Microstructure, Properties, and Materials, Fourth edition McGraw-Hill Companies, New York City, 2014. 641–652.
[2] Jeffrey J. Thomas, A new approach to modeling the nucleation and growth kinetics of tricalcium silicate hydration, J. Am. Ceram. Soc. 90 (10) (2007) 3282–3288.
[3] Jeffrey W. Bullard, Hamli M. Jennings, Richard A. Livingston, Andre Nonat, George W. Scherer, Jeffrey S. Schweitzer, Karen L. Scrivener, Jeffrey J. Thomas, Mechanisms of cement hydration, Cem. Concr. Res. 41 (12) (2011) 1208–1223.
[4] D.A. Silva, P.J. Monteiro, Hydration evolution of C_3S–EVA composites analyzed by soft X-ray microscopy, Cem. Concr. Res. 35 (2) (2005) 351–357.
[5] Jeffrey J. Thomas, Andrew J. Allen, Hamlin M. Jennings, Hydration kinetics and microstructure development of normal and $CaCl_2$-accelerated tricalcium silicate pastes, J. Phys. Chem. C 113 (46) (2009) 19836–19844.
[6] H.N. Stein, J.M. Stevels, Influence of silica on the hydration of $3CaO \cdot SiO_2$, J. Appl. Chem. 14 (8) (1964) 338–346.
[7] M. Avrami, Kinetics of phase change. I: general theory, J. Chem. Phys. 7 (12) (1939) 1103–1112.
[8] Harry F.W. Taylor, Cement Chemistry, Thomas Telford, 1997.
[9] S.A. Rodger, G.W. Groves, N.J. Clayden, C.M. Dobson, A study of tricalcium silicate hydration from very early to very late stages, In MRS Proceedings, 85, Cambridge University Press 1986, pp. 13–20.
[10] I.G. Richardson, Tobermorite/jennite- and tobermorite/calcium hydroxide-based models for the structure of C–S–H: applicability to hardened pastes of tricalcium silicate, β-dicalcium silicate, Portland cement, and blends of Portland cement with blast-furnace slag, metakaolin, or silica fume, Cem. Concr. Res. 34 (9) (2004) 1733–1777.
[11] Hamlin M. Jennings, Refinements to colloid model of C–S–H in cement: CM-II, Cem. Concr. Res. 38 (3) (2008) 275–289.
[12] Georgios Constantinides, Franz-Josef Ulm, The nanogranular nature of C–S–H, J. Mech. Phys. Solids 55 (1) (2007) 64–90.
[13] R. Taylor, Characterization of C–S–H in Early and Late Age Systems Containing AdmixturesDiss University of Leeds, 2010.
[14] R. Taylor, I.G. Richardson, R.M.D. Brydson, Composition and microstructure of 20-year-old ordinary Portland cement–ground granulated blast-furnace slag blends containing 0 to 100% slag, Cem. Concr. Res. 40 (7) (2010) 971–983.
[15] J. Ha, S. Chae, K.W. Chou, T. Tyliszczak, P.J.M. Monteiro, Effect of polymers on the nanostructure and on the carbonation of calcium silicate hydrates: a scanning transmission X-ray microscopy study, J. Mater. Sci. 47 (2) (2012) 976–989.
[16] Marie D. Jackson, Sejung R. Chae, Sean R. Mulcahy, Cagla Meral, Rae Taylor, Penghui Li, Unlocking the secrets of Al-tobermorite in Roman seawater concrete, Am. Mineral. 98 (10) (2013) 1669–1687.
[17] P.K. Mehta, D. Pirtz, M. Polivka, Properties of alite cements, Cem. Concr. Res. 9 (4) (1979) 439–450.
[18] J.R. Kremer, D.N. Mastronarde, J.R. McIntosh, Computer visualization of three-dimensional image data using IMOD, J. Struct. Biol. 116 (1996) 71–76.
[19] Dien Li, G.M. Bancroft, Kasrai Masoud, M.E. Fleet, X.H. Feng, K.H. Tan, B.X. Yang, High-resolution Si K- and $L_{2,3}$-edge XANES of α-quartz and stishovite, Solid State Commun. 87 (7) (1993) 613–617.
[20] S.J. Naftel, T.K. Sham, Y.M. Yiu, B.W. Yates, Calcium L-edge XANES study of some calcium compounds, J. Synchrotron Radiat. 8 (2) (2001) 255–257.
[21] Daniel Hernández-Cruz, Craig W. Hargis, Sungchul Bae, Pierre A. Itty, Cagla Meral, Jolee Dominowski, Michael J. Radler, David A. Kilcoyne, Paulo JM Monteiro, Multiscale characterization of chemical–mechanical interactions between polymer fibers and cementitious matrix, Cem. Concr. Compos. 4 (2014) 9–18.
[22] Image and spectra visualization and analysis, http://unicorn.mcmaster.ca/aXis2000.html.
[23] S.T. Bergold, F. Goetz-Neunhoeffer, J. Neubauer, Quantitative analysis of C–S–H in hydrating alite pastes by in-situ XRD, Cem. Concr. Res. 53 (2013) 119–126.
[24] Mireille Courtial, M.-N. De Noirfontaine, Frederic Dunstetter, Gilles Gasecki, Marcel Signes-Frehel, Polymorphism of tricalcium silicate in Portland cement: a fast visual identification of structure and superstructure, Powder Diffract. 18.01 (2003) 7–15.
[25] Jeffrey J. Thomas, Jeffrey J. Chen, Hamlin M. Jennings, Dan A. Neumann, Ca–OH bonding in the C–S–H gel phase of tricalcium silicate and white portland cement pastes measured by inelastic neutron scattering, Chem. Mater. 15 (20) (2003) 3813–3817.
[26] Karen L. Scrivener, Backscattered electron imaging of cementitious microstructures: understanding and quantification, Cem. Concr. Compos. 26 (8) (2004) 935–945.
[27] Geoffrey W. Groves, TEM studies of cement hydration, MRS Proceedings, vol. 85, Cambridge University Press, 1986.
[28] E. Lippmaa, M. Mägi, M. Tarmak, W. Wieker, A.R. Grimmer, A high resolution ^{29}Si NMR study of the hydration of tricalciumsilicate, Cem. Concr. Res. 12 (1982) 597–602.
[29] G.W. Groves, A. Brough, I.G. Richardson, C.M. Dobson, Progressive changes in the structure of hardened C_3S cement pastes due to carbonation, J. Am. Ceram. Soc. 74 (1991) 2891–2896.
[30] H. Taylor, P. Barret, P. Brown, D. Double, G. Frohnsdorff, V. Johansen, D. Ménétrier-Sorrentino, I. Odler, L. Parrott, J. Pommersheim, M. Regourd, J. Young, The hydration of tricalcium silicate, Mater. Struct. 17 (1984) 457–468.
[31] Hamlin M. Jennings, A model for the microstructure of calcium silicate hydrate in cement paste, Cem. Concr. Res. 30 (1) (2000) 101–116.

[32] I.G. Richardson, The calcium silicate hydrates, Cem. Concr. Res. 38 (2) (2008) 137–158.
[33] Sejung R. Chae, Juhyuk Moon, Seyoon Yoon, Sungchul Bae, Pierre Levitz, Robert Winarski, Paulo JM Monteiro, Advanced nanoscale characterization of cement based materials using X-ray synchrotron radiation: a review, Int. J. Concr. Struct. Mater. 7.2 (2013) 95–110.
[34] Paulo J.M. Monteiro, Laurence Clodic, Francesco Battocchio, Waruntorn Kanitpanyacharoen, Sejung Rosie Chae, Juyoung Ha, Hans-Rudolf Wenk, Incorporating carbon sequestration materials in civil infrastructure: a micro and nano-structural analysis, Cem. Concr. Compos. 40 (2013) 14–20.
[35] J. Ha, S. Chae, K.W. Chou, T. Tyliszczak, P.J.M. Monteiro, Scanning transmission X-ray microscopic study of carbonated calcium silicate hydrate, Transp. Res. Rec. 2142 (1) (2010) 83–88.
[36] Michael E. Fleet, Xiaoyang Liu, Calcium L2, 3-edge XANES of carbonates, carbonate apatite, and oldhamite (CaS), Am. Mineral. 94 (8-9) (2009) 1235–1241.
[37] S. Hanhan, A.M. Smith, M. Obst, A.P. Hitchcock, Optimization of analysis of soft X-ray spectromicroscopy at the Ca 2p edge, J. Electron Spectrosc. Relat. Phenom. 173 (1) (2009) 44–49.
[38] Dien Li, et al., Silicon K-edge XANES spectra of silicate minerals, Phys. Chem. Miner. 22 (2) (1995) 115–122.
[39] Li Dien, G.M. Bancroft, M. Kasrai, M.E. Fleet, R.A. Secco, X.H. Feng, K.H. Tan, B.X. Yang, X-ray absorption spectroscopy of silicon dioxide (SiO_2) polymorphs: the structural characterization of opal, Am. Mineral. 79 (1994) 622–632.
[40] Stefano Merlino, Elena Bonaccorsi, Thomas Armbruster, Tobermorites: their real structure and order–disorder (OD) character, Am. Mineral. 84 (1999) 1613–1621.
[41] E. Bonaccorsi, S. Merlino, H.F.W. Taylor, The crystal structure of jennite, $Ca_9Si_6O_{18}(OH)_{6.8}H_2O$, Cem. Concr. Res. 34 (9) (2004) 1481–1488.
[42] Sebastien Brisard, Rosie S. Chae, Isabelle Bihannic, Laurent Michot, Peter Guttmann, Jürgen Thieme, Gerd Schneider, Paulo JM Monteiro, Pierre Levitz, Morphological quantification of hierarchical geomaterials by X-ray nano-CT bridges the gap from nano to micro length scales, Am. Mineral. 97 (2-3) (2012) 480–483.
[43] Andrew J. Allen, Jeffrey J. Thomas, Hamlin M. Jennings, Composition and density of nanoscale calcium–silicate–hydrate in cement, Nat. Mater. 6 (4) (2007) 311–316.
[44] S. Bae, R. Taylor, D. Hernández-Cruz, S. Yoon, D. Kilcoyne, P.J. Monteiro, Soft X-ray Spectromicroscopic Investigation of Synthetic C-S-H and C3S Hydration Products, J. Am. Ceram, Soc, 2015.